Available online at www.sciencedirect.com
ScienceDirect
Trans. Nonferrous Met. Soc. China 32(2022) 750−764

Transactions of Nonferrous Metals Society of China
www.tnmsc.cn

Effects of Cd addition in welding wires on microstructure and mechanical property of wire and arc additively manufactured Al−Cu alloy

Ming-ye DONG[1], Yue ZHAO[1,2], Quan LI[3], Fu-de WANG[3], Ai-ping WU[1,2,4]

1. Department of Mechanical Engineering, Tsinghua University, Beijing 100084, China;
2. Key Laboratory for Advanced Materials Processing Technology, Ministry of Education, Tsinghua University, Beijing 100084, China;
3. Capital Aerospace Machinery Corporation Limited, Beijing 100076, China;
4. State Key Laboratory of Tribology, Tsinghua University, Beijing 100084, China

Received 19 March 2021; accepted 26 October 2021

Abstract: Wall structures were made by cold metal transfer-based wire and arc additive manufacturing using two kinds of ER2319 welding wires with and without Cd elements. T6 heat treatment was used to improve mechanical properties of these wall structures. Due to the higher vacancy binding energy of Cd, Cd-vacancy clusters are formed in the aging process and provide a large number of nucleation locations for θ' phases. The higher diffusion coefficient of the Cd-vacancy cluster and the lower interfacial energy of θ' phase lead to the formation of dense θ' phases in the heat-treated α(Al). According to the strengthening model, after adding Cd in ER2319 welding wires, the yield strength increases by 43 MPa in the building direction of the heat-treated wall structures.

Key words: Cd; welding wire; wire and arc additive manufacturing; Al−Cu alloy

1 Introduction

Modern large-scale complex aerospace structures are confronted with challenges of improving manufacturing efficiency and overall mechanical properties [1,2]. Compared with laser additive manufacturing (LAM) and electron beam additive manufacturing (EBAM), wire and arc additive manufacturing (WAAM) has great potential for the manufacturing of large-scale complex aerospace structures because of high deposition rate, low cost and flexibility [3−5]. Cold metal transfer (CMT)-based WAAM is a promising technology in high-performance, flexible energy input and spatter-free Al−Cu alloy manufacturing. It also has great potential to enable cost reduction and high-performance manufacturing compared with subtractive manufacturing methods [6−8].

Al−Cu alloy has gained more attention in the aerospace industries because of good weldability and mechanical properties. There were several studies about the microstructure and mechanical properties of wire and arc additively manufactured Al−Cu alloy in recent years [9,10]. ZHOU et al [11] made an as-deposited wire and arc additively manufactured 2219 Al alloy wall structure, but the yield strength and ultimate tensile strength only reached 182.9 MPa and 273.5 MPa in deposition direction, respectively. Therefore, heat treatment was frequently used to improve the mechanical properties. The microstructure and mechanical property of wire and arc additively manufactured Al−Cu large-scale complex structures were usually

---

Corresponding author: Quan LI, Tel: +86-10-68750239, E-mail: liquan_211@aliyun.com;
Ai-ping WU, Tel: +86-10-62773859, E-mail: wuaip@tsinghua.edu.cn

DOI: 10.1016/S1003-6326(22)65830-8

increased by T6 heat treatment instead of T8 heat treatment, which limited the increase of yield strength. Our previous research about wire and arc additively manufactured 2219 Al alloy found that the yield strength, ultimate tensile strength and elongation of T6-state wall structures in the building direction only reached 296 MPa, 371 MPa and 4.5%, which still needed to improve [12−14].

Therefore, the strengthening mechanism is worth to discuss. It is considered that the nanoscale metastable strengthening phase features such as the content, density, size and coherent relation mainly determined the strengthening effects [9,10,15]. Therefore, the scholars were dedicated to optimizing nanoscale metastable strengthening phase behaviors [16]. Cd has high vacancy binding energy and extremely low solubility in α(Al) [17]. It was proven that Cd could modify traditional precipitation sequences [18] and induced θ' phase precipitation in ZL205A alloy [19]. It was found that Cd decreased the interfacial energy between α(Al) and θ' phases, which promoted the precipitation of θ' phases [18,20]. In and Sn had similar strengthening effects. It was found that the formation of metastable nanoparticles in the early stage of the aging process provided more heterogeneous nucleation locations for θ' phases [21,22], but Cd has a higher melting point (321 °C), so it has great potential in increasing high-temperature mechanical properties and widening the range of application [23]. However, the effects of Cd addition in welding wire on the microstructure and mechanical properties of wire and arc additively manufactured 2219 Al alloy are still unclear. Therefore, the purpose of our research is to explore the effects of Cd addition in welding wires on the microstructure and mechanical properties of wire and arc additively manufactured 2219 Al alloy walls and to summarize the strengthening mechanism to optimize wire components.

In this work, wall structures were made by CMT-based WAAM using two kinds of ER2319 welding wires with and without Cd elements. T6 heat treatment was used on these wall structures after the WAAM deposition process. The microstructure and mechanical properties were discussed in detail. The microstructure was studied including grains, phase distribution, chemical composition and strengthening phase features. The mechanical properties were studied by tensile tests. A precipitation thermodynamics model and a dynamics model were used to analyze θ' phase precipitation behavior. A strengthening model was used to quantify the improvement of yield strength in the aging process. The results can be used as the basis for the chemical composition design of ER2319 welding wires.

2 Experimental

2.1 Materials

Two kinds of ER2319 welding wires with different chemical compositions were used. For convenience, ER2319 welding wire with Cd addition was marked as Sample 1, and ER2319 welding wires without Cd addition was marked as Sample 2. The diameter of these welding wires was 1.2 mm. The dimension of the 6061-T6 Al alloy substrate was 300 mm × 300 mm × 10 mm. Table 1 gives the nominal composition and measured chemical composition of Samples 1 and 2.

2.2 WAAM experiments and heat treatment process

The WAAM automated deposition system consists of a Fronius CMT R4000 heat source, a wire feeding system, a six-axle welding robot and

Table 1 Chemical composition of ER2319 welding wires (wt.%)

Sample No.	Composition type	Cu	Si	Fe	Mn	Zn	Ti	Mg	Zr	V	Cd	Al
1	Nominal	5.80−6.80	≤0.20	≤0.30	0.20−0.40	≤0.10	0.10−0.20	≤0.02	0.10−0.20	0.05−0.15	0.05−0.25	Bal.
	Measured	6.10	0.08	0.02	0.30	0.01	0.10	0.02	0.13	0.13	−	Bal.
2	Nominal	5.80−6.80	≤0.20	≤0.30	0.20−0.40	≤0.10	0.10−0.20	≤0.02	0.10−0.20	0.05−0.15	−	Bal.
	Measured	6.40	0.05	0.11	0.28	0.01	0.11	0.003	0.14	0.12	−	Bal.

*The measured Cd content was not given because of the patent protection its control system. Before the WAAM experiments, the substrates were scrubbed by a steel brush and cleaned by acetone to remove oxide and grease, and the welding wires were fully dried. The dimension of the wall structures was about 180 mm (height) × 90 mm (length) × 22 mm (thickness). The thickness of each layer was about 2.5 mm. There were two passes in each layer in order to gain the required width, and the weave frequency and amplitude were set for each pass. Adjacent passes in the same layer were deposited in the same direction, and layers at adjacent height were deposited in the adverse direction. The WAAM experimental parameters are listed in Table 2. Arc voltage and current are not listed because these parameters were gained automatically by the CMT expert database. The value of CMT/pulse represents the ratio of CMT number to pulse number in one cycle. The change of CMT/pulse value can adjust heat input flexibly. High-purity pure argon (99.99%) was used as the shielding gas, and the constant flow was 25 L/min. The interlayer cooling time was 60 s.

The sampling positions of the tensile samples and metallographic specimens for observation and microhardness tests are shown in Fig. 1. After being cut from the substrates, the as-deposited wall structures were put into a muffle furnace for T6 treatment. The heat treatment curve is shown in Fig. 2. All as-deposited wall structures were firstly heated to 535−540 °C for 90 min followed by water quenching. Next, the wall structures were heated to 175 °C for 180 min and cooled inside the furnace to room temperature [13]. Then, the tensile samples both in the deposition direction and building direction were cut from T6-state wall structures for the tensile tests. The WAAM experimental parameters in Table 2 and heat treatment parameters in Fig. 2 were kept consistently no matter which kind of ER2319 welding wire was used in the WAAM experiments.

2.3 Testing procedure

The dimension of the samples for microstructure observation and microhardness tests was 20 mm × 20 mm × 10 mm. After being cut by EDM, samples were ground with 80, 400, 1000 and 3000 waterproof abrasive papers in turn and then polished with 0.5 μm diamond paste to a mirror surface. An ultrasonic cleaning machine was used to clean up contaminants after grounding and polishing. Keller’s reagent (2.5 mL HNO_3 + 1.5 mL HCL + 1 mL HF + 95 mL H_2O) was used for corrosion tests. Samples were submerged and held for 8−10 s in Keller’s reagent. X-ray fluorescence (XRF) was used to measure the element content of the welding wires. Optical microscopy (OM) was used to observe microstructure features and measure the average thickness of the interlayer regions and intra-layer regions along the building direction. Microstructure and fracture surfaces were observed by scanning electron microscopy (SEM). The phase chemical composition analysis was performed with energy disperse spectroscopy (EDS). The phase type analysis was performed by X-ray diffraction (XRD). Samples with a dimension of 10 mm × 10 mm × 0.5 mm were cut by EDM followed by ion polishing to a nanoscale thickness. Observation of nanoscale strengthening phases in α(Al) was performed by transmission electron microscope (TEM), and the acceleration voltage

Table 2 WAAM experimental parameters

Wire feeding speed/ $(m\cdot min^{-1})$	Travel speed/ $(mm\cdot s^{-1})$	CMT/pulse	Weave frequency/Hz	Weave amplitude/mm	Pass space/mm
9	7	7/25	3	5	7

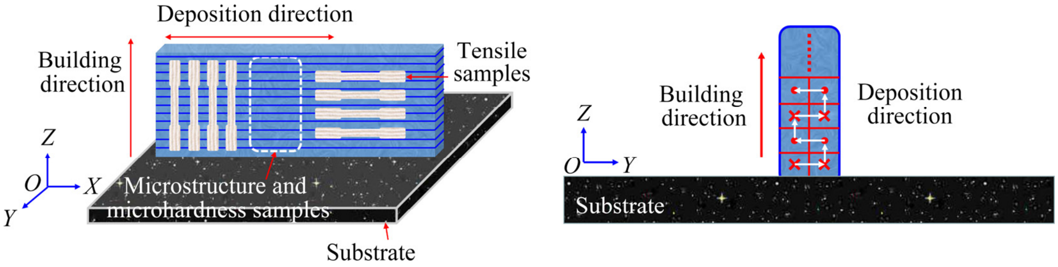

Fig. 1 Position of tensile samples, metallographic specimens and deposition pattern

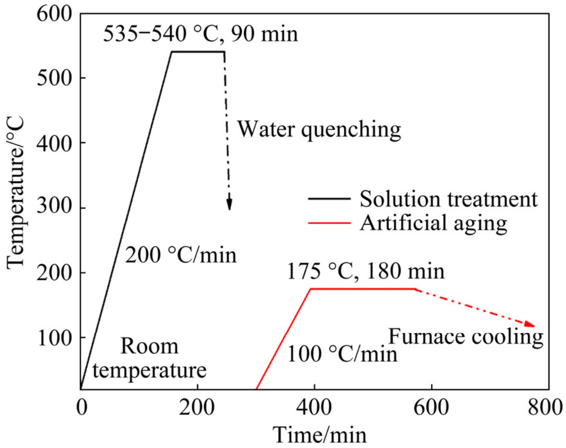

Fig. 2 Heat treatment process curve

was 200 kV. Image-Pro Plus software was used to quantify the number and size of the precipitated phases in α(Al).

Microhardness was examined by a Vickers hardness tester. The test load and holding time were 0.98 N and 10 s, respectively. The values of Vickers hardness were automatically acquired by the software calculation. Round bar tensile samples with a diameter of 5 mm were prepared for tensile tests both in the deposition direction and building direction. Tensile tests were performed with a constant quasi-static velocity of 2 mm/min. Mechanical properties were averaged results of four tensile samples.

3 Results and discussion

3.1 Microstructure

Figure 3 shows the typical OM images after T6 heat treatment. As reported in our previous work [12], the wall structure could be divided into the bottom, middle and top regions. The area of the top region and the bottom region was very small, and these regions were usually machined. Thus, in this work, the samples for microstructure observation and tensile tests were all taken from the middle region of the wall structures. By comparing Figs. 3(a, c, e, g) with Figs. 3(b, d, f, h), there are some similar features. The layer characteristics due to the layer-by-layer WAAM process were clear, and there were boundaries between the interlayer regions (about 0.5 mm thick along building direction according to the average measurement results in the optical microscope) and intra-layer regions (about 2.0 mm thick along building direction). The grain size in the interlayer regions was less than that in the intra-layer regions, and there were more second phases in the interlayer regions. Also, the second phase distribution was discontinuous because the eutectic structures dissolved in the solution process. There were also some differences between Sample 1 and Sample 2. As for grain size, typical OM images (with a size of 0.5 mm × 0.5 mm) of each sample were used for the quantitative analysis to calculate the average grain size. Ten images were randomly selected both in the interlayer regions and intra-layer regions. In each image, three lines along the building direction and three lines perpendicular to the building direction with the same length were used. The grain number was recorded and the grain size was averaged. Results showed that the average grain size in the interlayer region and intra-layer region of Sample 1 was 17 and 48 μm, respectively. The average grain size in interlayer region and intra-layer region of Sample 2 was 18 and 62 μm, respectively.

Figure 4 shows the typical SEM images of Samples 1 and 2. Boundaries were clear between the interlayer regions and the intra-layer regions. Phase distribution features were distinctly different in the interlayer regions and intra-layer regions. The second phases were more likely to concentrate in the interlayer regions. After T6 heat treatment, large amounts of eutectic structures dissolved. Cu adequately diffused and nanoscale phases were formed in α(Al). Thus, discontinuous second phases distributed along the grain boundaries or were embedded in grains. Moreover, more second phases with irregular shapes existed in Sample 2, while fewer second phases with approximate round shape existed in Sample 1. EDS results in Fig. 4 are given in Table 3. The compositions of Points A and B in Sample 1 were nearly in general agreement with Al_2Cu. Al_2Cu (Point D) was also found in Sample 2. Meanwhile, the Fe-rich phase (Point E) was also detected. Cd was detected in α(Al) of Sample 1. XRD patterns are shown in Fig. 5. The phase type in Fig. 5 basically matched with EDS results in Table 3. α(Al) and Al_2Cu were the main phases in Samples 1 and 2. There was no diffraction peak of the Fe-rich phase in Sample 1, but it can be detected in Sample 2. The difference in Fe-rich phase amount can be attributed to the chemical composition of welding wires (Table 1). The content of impurity elements especially Fe was

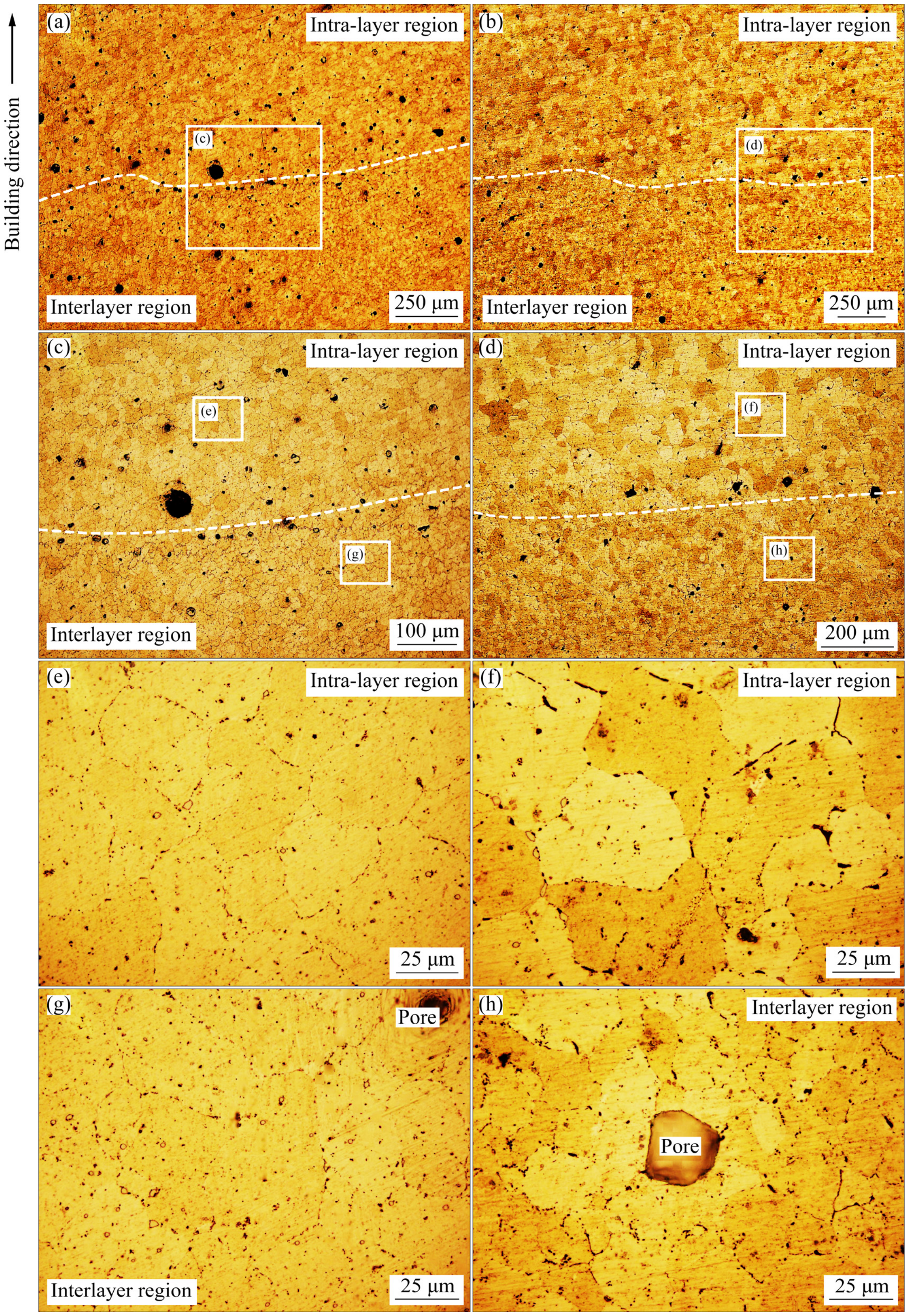

Fig. 3 Typical OM images of Sample 1 (a, c, e, g) and Sample 2 (b, d, f, h)

close to zero in Sample 1. Therefore, under the condition of the same deposition parameters and heat treatment parameters, the amount of Fe-rich phases in Sample 1 was lower than that in Sample 2. Moreover, because of more second phases in Sample 2 (Fig. 4(b)), the boundary between the interlayer region and the intra-layer region was not clearer than that in Sample 1 (Fig. 4(a)).

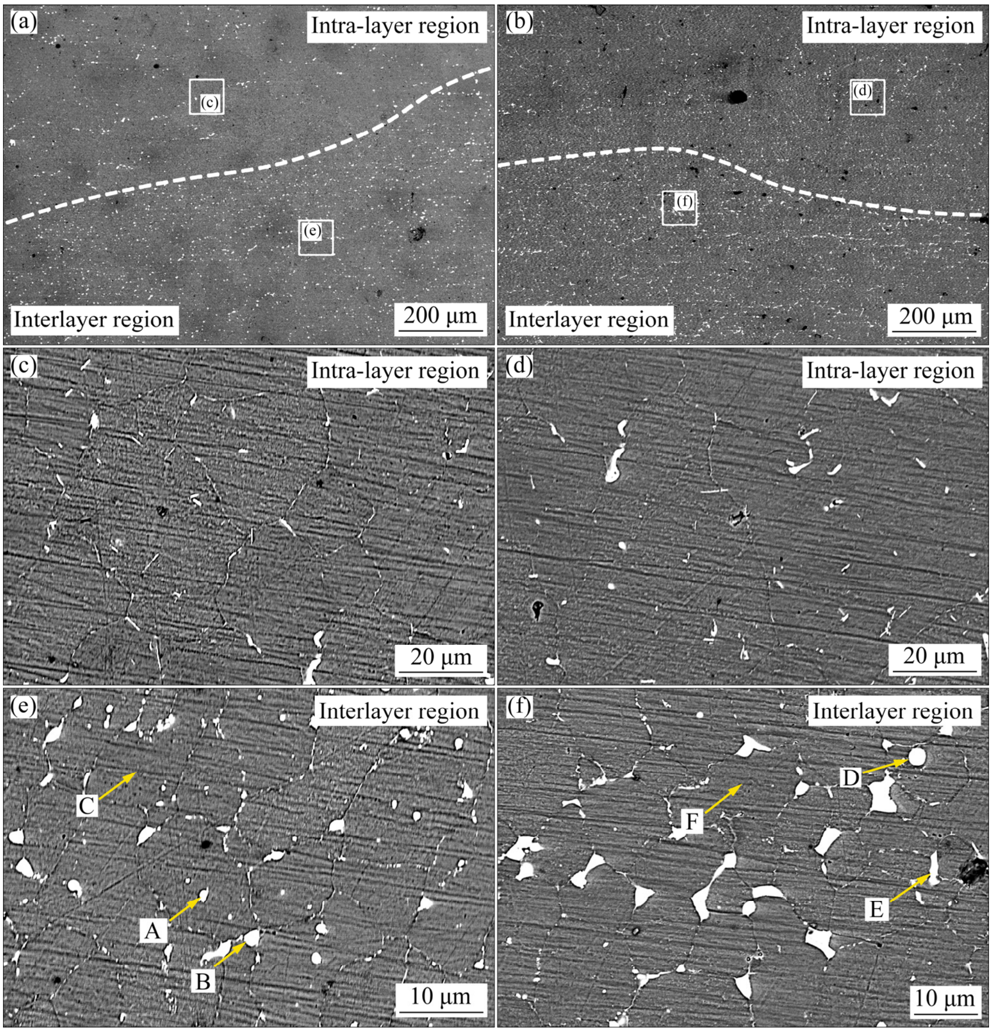

Fig. 4 Typical SEM images of Sample 1 (a, c, e) and Sample 2 (b, d, f)

Table 3 EDS results of measuring points in Fig. 4 (at.%)

Measuring point	Al	Cu	Fe	Mn	Cd	Possible phase
A	64.59	35.41	0.00	0.00	0.10	Al_2Cu
B	66.95	33.05	0.00	0.00	0.00	Al_2Cu
C	95.98	3.86	0.00	0.00	0.16	α(Al)
D	65.43	34.57	0.00	0.00	0.00	Al_2Cu
E	65.27	18.94	9.62	6.17	0.00	Fe-rich phase
F	95.62	4.38	0.00	0.00	0.00	α(Al)

3.2 Mechanical properties

The microhardness distribution along the building direction in the centerline of the middle part in the wall structure is shown in Fig. 6. In Vickers hardness tests, there were 20 measuring points with 1 mm interval between two measuring points. The average microhardness values of Samples 1 and 2 were HV 151 and HV 143, respectively. Table 4 shows average yield strength (YS), ultimate strength (UTS) and elongation of Samples 1 and 2 both in the deposition direction and building direction. Compared with Sample 2, the yield strength in the deposition direction and building direction of Sample 1 increased by 5.5% and 9.3%, respectively. It is worth noting that the ultimate strength of Sample 1 decreased by 5.0% in the deposition direction and increased by 2.3% in the building direction. The Cd addition sacrificed

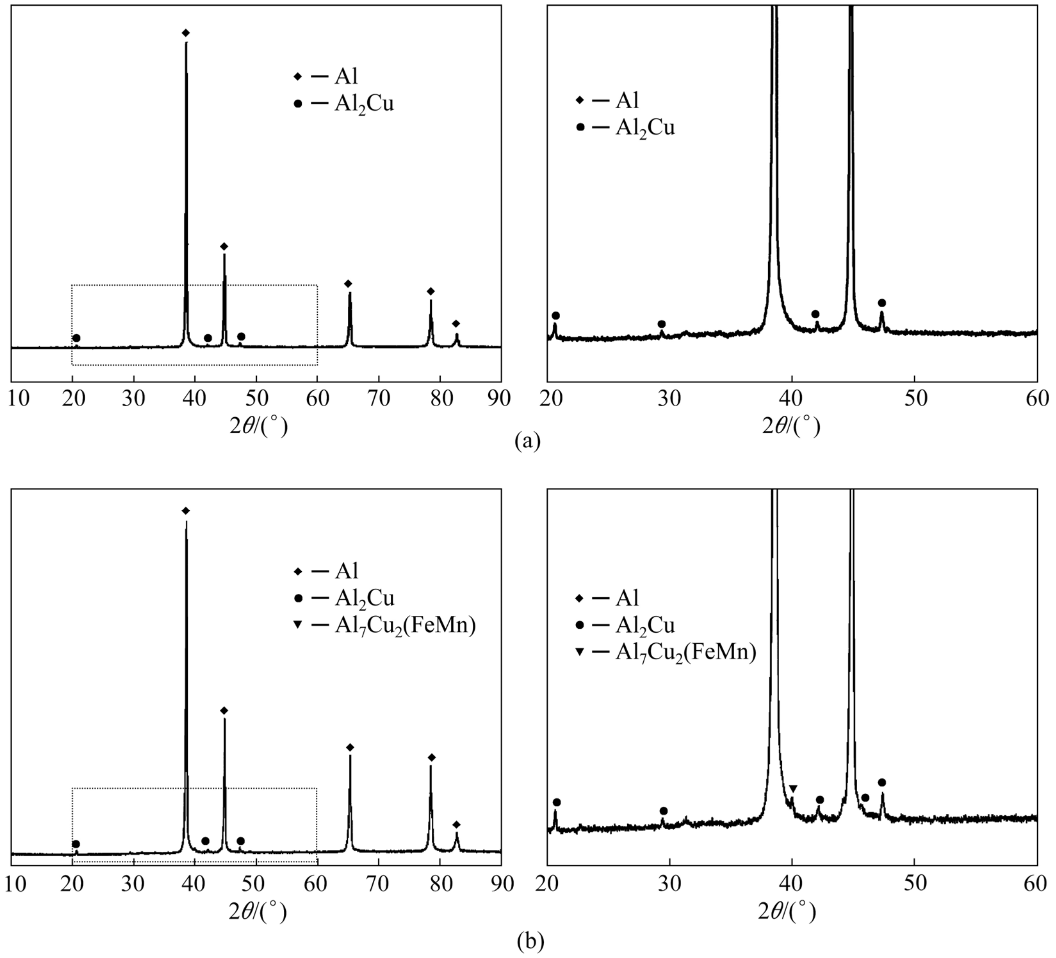

Fig. 5 XRD patterns of Sample 1 (a) and Sample 2 (b)

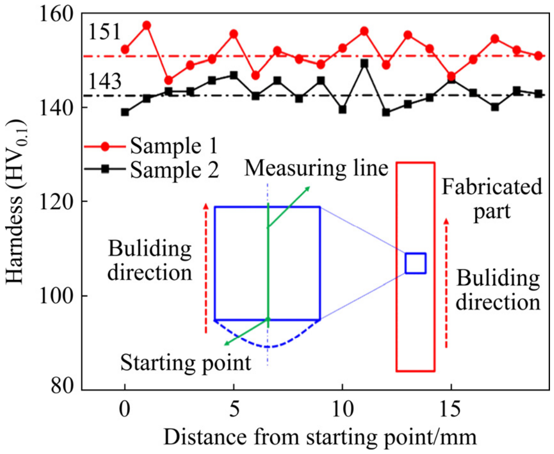

Fig. 6 Microhardness test results

plasticity to some extent. The elongations in the deposition direction and in the building direction of Sample 1 were decreased by 52.0% and 20.7%, respectively.

Table 4 Average mechanical properties

Sample No.	Test direction	UTS/ MPa	YS/ MPa	Elongation/ %
1	Deposition	435	316.5	8.3
	Building	433.5	323.5	7.3
2	Deposition	457.7	300	17.3
	Building	425.7	296	9.2

Figure 7 shows the typical fracture surfaces of Samples 1 and 2 both in the deposition direction and building direction. As for the cracked second phases, Table 5 lists the corresponding EDS results of measuring points in Fig. 7. There were more pores on the fracture surface in the building direction in Sample 1, and the cracked phases were mainly Al_2Cu. There were fewer pores in Sample 2, and some Fe-rich cracked phases were detected besides cracked Al_2Cu. The composition of these Fe-rich phases was similar to $Al_7Cu_2(FeMn)$. These Fe-rich phases were formed during the WAAM solidification process. Solution and aging temperatures could not reach their phase transformation points [24]. It was also found that these brittle phases damaged mechanical property more greatly than Al_2Cu and eutectic structures [25].

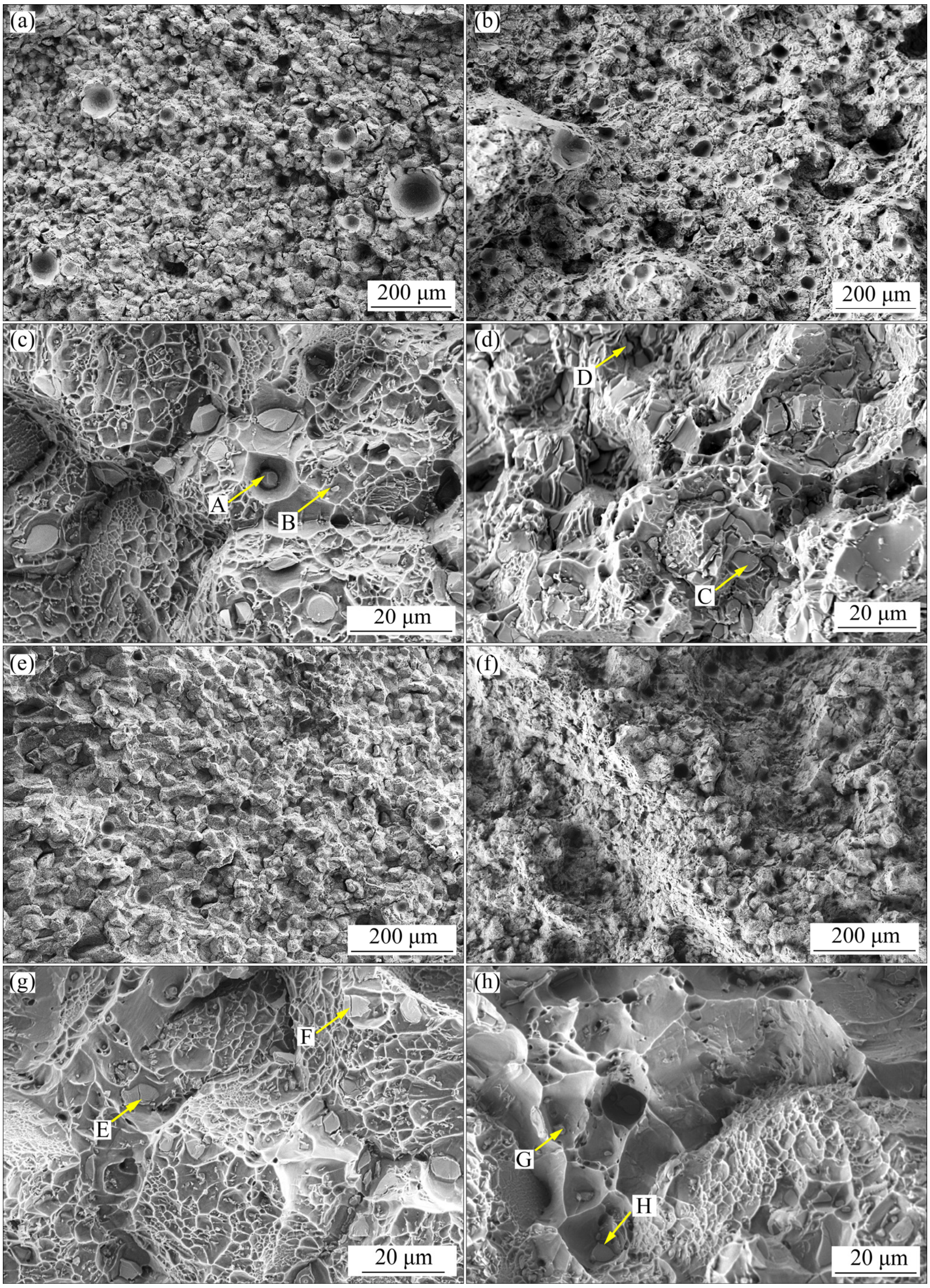

Fig. 7 SEM images of fracture surface: (a, c) Sample 1 in building direction; (b, d) Sample 2 in building direction; (e, g) Sample 1 in deposition direction; (f, h) Sample 2 in deposition direction

Fe-rich phases were likely to become the initiation points in the tensile tests, which decreased the ductility.

There were typical intergranular fracture characteristics in Sample 1, and the dimples on the grain surface were small and shallow. This illustrated lower grain boundary strength. There were partial intergranular fracture characteristics in Sample 2, but bigger and deeper dimples were also observed, which indicated better ductility. As for fractures in the deposition direction, there were similar intergranular fracture characteristics and dimple features in Sample 1 compared with that in the building direction. Therefore, there was small mechanical property anisotropy in Sample 1. However, a large amount of deeper dimples, bright torn edges and less cracked second phases were observed in Sample 2 compared with that in the

Table 5 EDS results of measuring points in Fig. 7 (at.%)

Measuring point	Al	Cu	Fe	Mn	Cd	Possible phase
A	67.13	32.18	0.00	0.00	0.66	Al_2Cu
B	65.09	34.54	0.00	0.00	0.27	Al_2Cu
C	61.28	38.72	0.00	0.00	0.00	Al_2Cu
D	70.24	14.32	9.28	6.16	0.00	Fe-rich phase
E	65.89	33.98	0.00	0.00	0.13	Al_2Cu
F	64.77	34.54	0.00	0.00	0.69	Al_2Cu
G	68.48	18.10	8.64	4.78	0.00	Fe-rich phase
H	66.02	33.98	0.00	0.00	0.00	Al_2Cu

building direction. Moreover, area of intergranular features decreased. Thus, fractures in the deposition direction of Sample 2 showed better ductility. Therefore, there was obvious mechanical property anisotropy in Sample 2. In our previous work [12], we concluded that the concentrated brittle phases in the interlayer regions were weaker parts. The tensile force had a different orientation relationship with the interlayer regions in the building direction and deposition direction. Thus, there was mechanical property anisotropy in the heat-treated wall structures. As for Sample 1 welding wire, the measured impurity element content (Table 1) was lower than that in Sample 2 welding wire, and the amount of Fe-rich phases in the interlayer regions was also lower (Fig. 4). Therefore, there was small mechanical property anisotropy including strength and elongation in Sample 1. Combined with the welding wire composition and fracture observation, it can be inferred that heat-treated mechanical property anisotropy was irrelative to the Cd addition. The reason of mechanical property anisotropy needs to be explored further.

3.3 Strengthening mechanism of Cd addition in Al−Cu WAAM alloy

The yield strength of Al−Cu alloy is mainly determined by Cu content and precipitation phase behavior in α(Al) [9]. According to the EDS results in Table 3 and average mechanical properties in Table 4, the Cd addition played an important role in the mechanical property improvement. Therefore, the strengthening mechanism was worth to discuss.

Figure 8 shows the typical images of precipitated phases and corresponding SAED images of Samples 1 and 2. There were dense needle-like phases with a length of about 200 nm in Sample 1, and some tiny round phases distributed uniformly in α(Al) or near needle-like phases (Figs. 8(a, b)). However, there were three kinds of precipitated phases in Sample 2. Most precipitated phases in Sample 2 were needle-like phases with a length of about 25 nm (Figs. 8(c, d)). Moreover, a small number of needle-like phases were similar to those in Sample 1 (Fig. 8(e)), and thick clubbed phases (Fig. 8(d)) were also observed in α(Al). To analyze the precipitated phase type in Fig. 8, the SAED images of α(Al) under the zone axis of [001] were added in Figs. 8(b, c). Compared with the SAED results in other works [11,26], there were diffraction patterns of the θ' phase in Sample 1, but they cannot be found in Sample 2. Table 6 lists EDS results of measuring points in Fig. 8. The needle-like phase (Point A) and round phase (Point B) in Sample 1 were approximately in general agreement with θ' phase and Cd, respectively. The EDS results of Point B included Al and Cu elements because of insufficient instrument resolution. According to the precipitated phase composition comparison [15], the needle-like phases (Points C and D) and the thick clubbed phase (Point E) were approximately in general agreement with θ'' phase, θ' phase and θ phase, respectively. Under the condition of same heat treatment parameters, the precipitated phase distribution illustrated insufficient aging in Sample 2 but relatively sufficient aging in Sample 1. To further confirm the precipitated phase type in α(Al) in Sample 1, Fig. 9 shows the typical HRTEM images under the zone axis of [001] and corresponding FFT images. The precipitated phase had a semi-coherent relation with α(Al) (Figs. 9(a, b)), which could be determined as θ' phase [22].

Five images of Sample 1 (Fig. 8(a)) and five images of Sample 2 (Fig. 8(c)) were selected to quantify the number and length of needle-like phases, as shown in Fig. 10. The length of most precipitated phase distributed in the range of 100−300 nm in Sample 1 and 10−30 nm in Sample 2. To conclude, the Cd addition was beneficial to the precipitation of θ' phases.

It was found that Cd existed in the form of elementary substance and primarily worked in the early aging process [19]. In order to analyze the effect of Cd addition, the difference of θ' phase precipitation behavior between Al−Cu alloy and

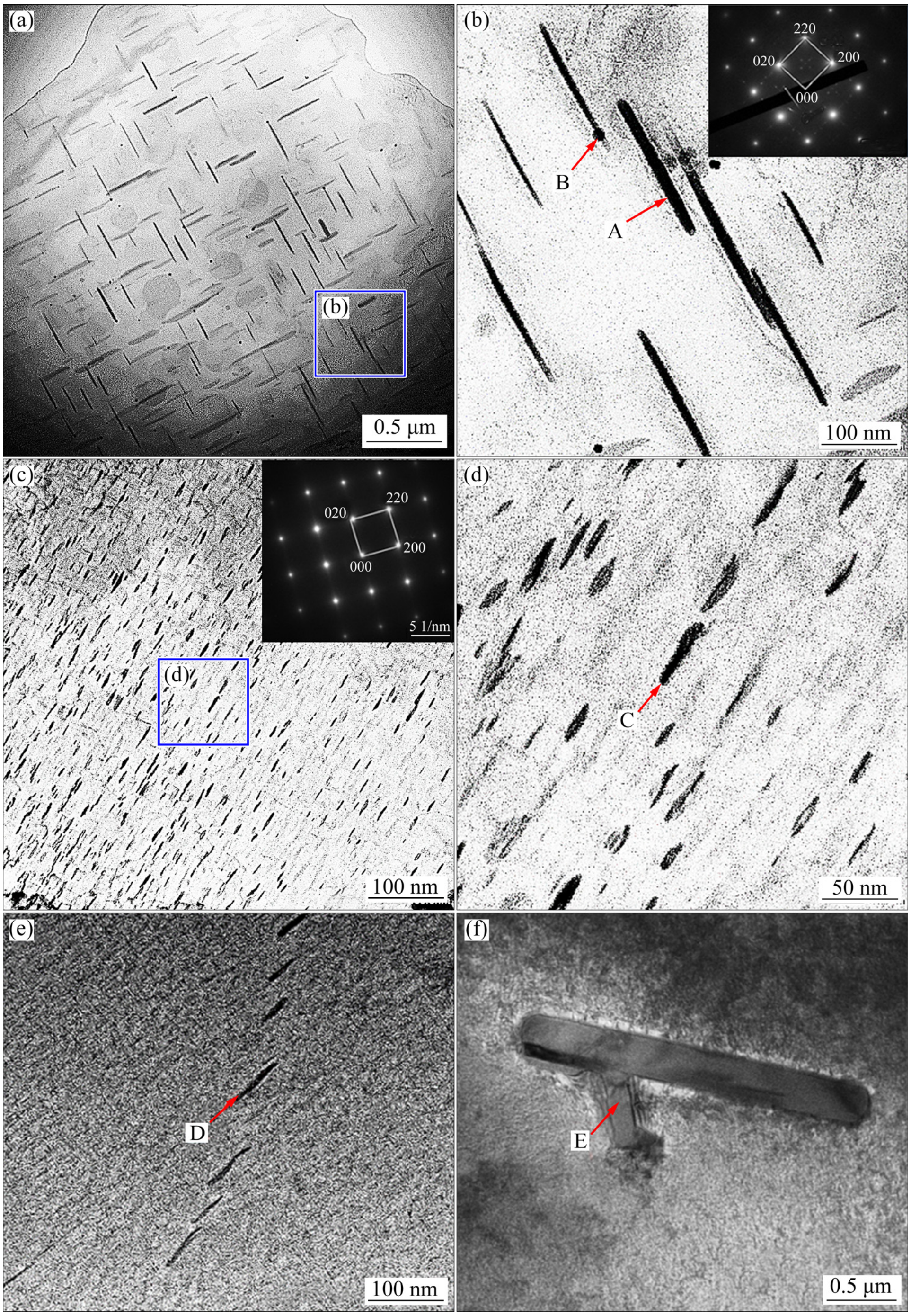

Fig. 8 Typical images of precipitated phases and corresponding SAED images in Samples 1 (a, b) and 2 (c, d, e, f)

Table 6 EDS results of measuring points in Fig. 8 (at.%)

Measuring point	Al	Cu	Cd	Possible phase
A	70.28	29.72	0	θ' phase
B	14.84	4.92	80.24	Cd
C	80.24	19.76	0	θ'' phase
D	70.99	29.01	0	θ' phase
E	66.92	33.08	0	θ phase

Al−Cu−Cd alloy was compared using precipitation thermodynamics and dynamics model, and the strengthening model was used to quantify the increase of aging strengthening.

During the diffusion process in aging, larger system free energy change promotes nanoscale metastable phase precipitation. The thermodynamic condition of precipitation in Al−Cu alloy and Al−Cu−Cd alloy are expressed as [27]

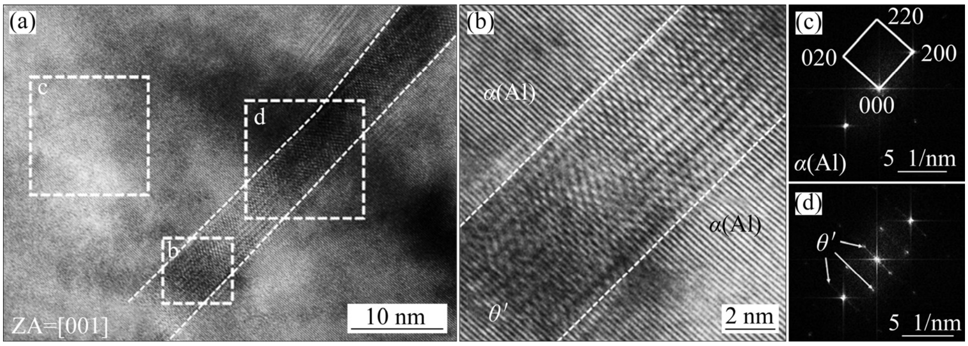

Fig. 9 Typical HRTEM images and corresponding FFT images in Sample 1

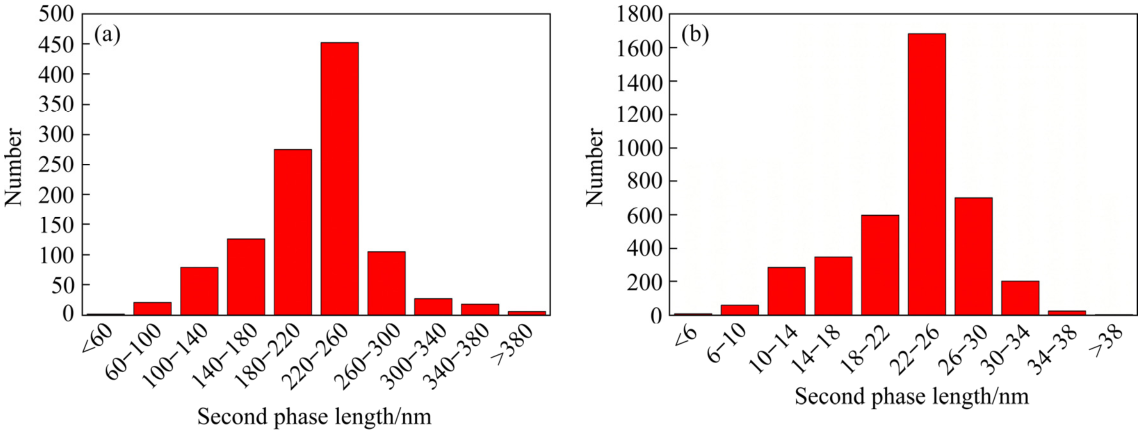

Fig. 10 Quantitative statistics results of precipitates in Sample 1 (a) and Sample 2 (b)

$$\Delta G_{\text{Al-Cu}}=-V_{\text{d}}\left(\Delta G_{\text{V}}-\Delta G_{\text{S}}\right)+S_{\text{d}}\gamma_{\text{d}}<0 \tag{1}$$

$$\Delta G_{\text{Al-Cu-Cd}}=-V_{\text{d}}\left(\Delta G_{\text{V}}-\Delta G_{\text{S}}\right)+S_{\text{d}}\gamma_{\text{d}}+F(V_{\text{Cd}},S_{\text{Cd}})<0 \tag{2}$$

where $\Delta G_{\text{Al-Cu-Cd}}$ and $\Delta G_{\text{Al-Cu}}$ are the Gibbs system free energy changes (the Gibbs free energy of the reactants minus that of the products) of Al−Cu−Cd alloy and Al−Cu alloy, respectively. V_{d} and S_{d} are the volume and area of the precipitated phase, respectively. ΔG_{v} is the volume free energy difference between the precipitated phase and α(Al). ΔG_{S} is the strain energy difference between the precipitated phase and α(Al). γ_{d} is the interfacial energy of the precipitated phase. $F(V_{\text{Cd}},S_{\text{Cd}})$ is an energy function of Cd which influences the Gibbs system free energy change. According to Fig. 8, Cd can be regarded as a spherical phase with a diameter of about 10 nm. The volume and area of θ′ phase are respectively 500 times and 125 times those of Cd. The $F(V_{\text{Cd}}, S_{\text{Cd}})$ term can be omitted. Therefore, the system free energy change equation is regarded as the same in Al−Cu alloy and Al−Cu−Cd alloy. However, γ_{d} in Al−Cu alloy (0.493 J/m^2) is higher than that in Al−Cu−Cd alloy (0.334 J/m^2) [20]. Therefore, the resistance item of interfacial energy ($S_{\text{d}}\gamma_{\text{d}}$) in Al−Cu−Cd alloy is lower. By considering the θ′ phase as the primary strengthening phase [15,16], as shown in Fig. 9, there were dense θ′ phases in Sample 1. The item of the difference between the volume free energy change and the strain energy change ($\Delta G_{\text{V}}-\Delta G_{\text{S}}$) in Al−Cu−Cd alloy is higher. Thus, $\Delta G_{\text{Al-Cu-Cd}}$ is lower than $\Delta G_{\text{Al-Cu}}$. The θ′ phases are more likely to form in Al−Cu−Cd alloy.

By considering the precipitation dynamics model of needle-like θ′ phase, the nucleation rate and Gibbs system free energy change are expressed as [23]

$$J=J_0\exp\left[-\left(\frac{A}{RT_{\text{M}}}\right)^3\frac{1}{\ln\left(C_{\text{m}}/C_{\text{e}}\right)}\right]\exp\left(-\frac{Q_{\text{d}}}{RT_{\text{M}}}\right) \tag{3}$$

$$\Delta G=-2\pi r^2h\Delta G_0+4\pi rh\gamma+2\pi r^2\gamma \tag{4}$$

where J is the nucleation rate and J_0 is its coefficient. T_{M} is the aging temperature. C_{m} and C_{e} are the mean molar concentrations of solute atoms at one certain moment and the equilibrium state, respectively. Q_d is the activation energy of the Cu-vacancy cluster. A and R are the constants for a certain composition and state of 2xxx series Al−Cu alloy. ΔG is the Gibbs system free energy change. ΔG_0 is the driving force change per volume. γ is the average interfacial energy of θ' phase. h and r are half the thickness and the radius of θ' phase, respectively.

The critical nucleation radius is expressed as

$$r_c=\frac{2\gamma(r/h+2)}{3\Delta G_0} \tag{5}$$

When the radius of θ' phase exceeds r_c, θ' phases spontaneously grow up. Before the peak aging, the radius of θ' phase is expressed as [27]

$$r=\frac{2r/h}{3(\alpha Dt)^{0.5}} \tag{6}$$

where D is the diffusion coefficient which mainly influences the diffusion process, and D is expressed as

$$D=D_0\exp(-\frac{Q_M}{RT_M})\exp(-\frac{Q_F}{RT_F}) \tag{7}$$

D_0 is a constant in the diffusion coefficient equation. T_F is solution temperature. Q_M, which represents the diffusion activation energy, mainly determines the value of D. Q_M of the Al−Cu−Cd alloy (13508 J/mol) was found to be lower than that of the Al−Cu alloy (55961 J/mol) [20]. Then, a large number of Cd-vacancy clusters were formed and provided plenty of nucleation locations for θ' phases, which decreased the nucleation energy of θ' phases.

According to the above analysis, the higher diffusion coefficient, higher driving force and lower interfacial energy in Al−Cu−Cd alloy promoted nucleation and growth of θ' phases. Thus, dense θ' phases were observed in Sample 1. However, there were fewer θ' phases in Sample 2, which illustrated that Sample 2 was not adequately strengthened under the condition of the same heat treatment parameters.

Bu considering the strengthening model of 2xxx series alloy, the yield strength of Al−Cu alloy can be expressed as [28]

$$\sigma_{\text{Al alloy}}=\sigma_0+\sigma_{\text{grain}}+\sigma_{\text{dislocation}}+\sigma_{\text{solution}}+\sigma_{\text{aging}} \tag{8}$$

σ_0 is the inherent strength of Al alloy. σ_{grain}, $\sigma_{\text{dislocation}}$, σ_{solution} and σ_{aging} are the contributions of grain size, dislocations, solution elements and the interaction between dislocation and precipitated phases to the strength, respectively. Each item can be expressed as [17,20,29,30]:

$$\sigma_0=\text{Constant} \tag{9}$$

$$\sigma_{\text{grain}}=A_0d^{-0.5} \tag{10}$$

$$\sigma_{\text{solution}}=MGb\varepsilon^{-0.5}C_{\text{Cu}}^{-0.5} \tag{11}$$

$$\sigma_{\text{dislocation}}=0 \tag{12}$$

$$\sigma_{\text{aging}}=\begin{cases} 2\beta GbM\left(\dfrac{2Af_v\sin 54.7°}{\sqrt{3}\pi}\right)^{0.5}\left(\dfrac{r_{\text{peak}}^{1.5(m-1)}}{r_c^{1.5m}}\right)r_m^{0.5}, \\ \qquad r_m<r_{\text{peak}} \\ 2\beta GbM\left(\dfrac{2Af_v\sin 54.7°}{\sqrt{3}\pi}\right)^{0.5}\left(\dfrac{r_m^{1.5m-1}}{r_c^{1.5m}}\right), \\ \qquad r_{\text{peak}}<r_m<r_t \\ 2\beta GbM\left(\dfrac{Af_v\sin 54.7°}{\pi}\right)^{0.5}\left(\dfrac{r_m^{m-1}}{r_c^{m}}\right), \\ \qquad r_t<r_m<r_c \\ 2\beta GbM\left(\dfrac{Af_v\sin 54.7°}{\pi}\right)^{0.5}\left(\dfrac{1}{r_c^{m}}\right),\ r_c<r_m \end{cases} \tag{13}$$

where A_0 is the coefficient of Hall−Patch equation. M, G and b are the mean orientation factor, shear modulus and magnitude of Burgers vector, respectively. ε is the lattice distortion in α(Al), and C_{Cu} is the Cu content in α(Al). β is the tension coefficient of dislocation. f_v is the volume fraction of plate-shaped precipitates. r_m is the mean precipitate radius. r_{peak} is the mean precipitate radius at peak aging and r_c is the mean radius at the start of the Cd release stage. r_t is the critical radius for the shear characteristic transformation between the precipitated phase and dislocations. Generally, r_{peak} is 0.8 times of r_t.

σ_0 equals 10 MPa and A_0 equals 68 MPa·μm$^{0.5}$. According to the grain size measurement results in Fig. 3, σ_{grain} values in the interlayer region and intra-layer region of Sample 1 are 16.49 and 9.82 MPa, respectively. σ_{grain} values in the interlayer region and intra-layer region of Sample 2 are 16.02 and 8.64 MPa, respectively. But ε cannot be quantified. LUO et al [31] used $\Delta\sigma_{\text{solution}}$ as a quantitative relation between the mass percentage of Cu and σ_{solution}, which can be expressed as

$$\Delta\sigma_{\text{solution}}=13.8\ \text{MPa}\cdot(\text{wt.\%})^{-1} \tag{14}$$

According to the EDS results in Table 3, σ_{solution} values of Samples 1 and 2 in the interlayer region are 119.35 and 135.16 MPa, respectively. After T6 heat treatment, residual stress created in the WAAM experiments was released, so $\sigma_{\text{dislocation}}$ is considered as zero. Because of the complicated relationship between dislocations and precipitated phases during the tensile process, some critical parameters could not be accurately confirmed in Al−Cu−Cd alloy. So, the yield strength data of building direction in Table 4 were used to infer the value of σ_{aging}, which can be expressed as

$$\sigma_{\text{aging}}=\sigma_{\text{Al alloy}}-\sigma_0-\sigma_{\text{grain}}-\sigma_{\text{dislocation}}-\sigma_{\text{solution}} \tag{15}$$

As for mechanical properties in the building direction, σ_{aging} values of Samples 1 and 2 are about 178 and 135 MPa, respectively. After adding Cd in ER2319 welding wires, the yield strength increases by 43 MPa in the building direction of the heat-treated wall structures.

According to the above analysis, Fig. 11 shows the schematic diagram of the aging sequence in Al−Cu alloy and Al−Cu−Cd alloy. To minimize the nucleation resistance during the aging process, different types of nanoscale metastable phases were formed in order. The traditional aging sequence of Al−Cu alloy was summed as follows: supersaturated solid solution (SSSS) → GP zone → θ'' phase → θ' phase → θ phase [15]. After adding Cd in the welding wires, the aging sequence was changed partially. Cd was easily combined with the supersaturated vacancy in the initial aging process because of higher vacancy binding energy (0.43 eV) compared with that of Cu (0.05 eV) [19,32]. The Cd-vacancy clusters were formed with a higher diffusion coefficient and restrained the formation of GP zone and θ'' phase because most vacancies were occupied and could not transport Cu atoms to the location for forming GP zone and θ'' phase [31]. Thus, the aging sequence of Al−Cu−Cd alloy could be summed as SSSS → Cd-vacancy cluster → θ' phase → θ phase.

4 Conclusions

(1) The yield strengths of heat-treated Al−Cu−Cd alloy prepared by WAAM in the building direction and deposition direction are 323.5 MPa and 316.5 MPa, respectively. Without Cd in ER2319 welding wires, cracked Fe-rich phases are detected in the fracture surface, and a large amount of deeper dimples are also observed. After adding Cd in ER2319 welding wires, there are clear intergranular fracture characteristics with small and shallow dimples on the grain surface, and cracked Al_2Cu can also be detected in the fracture surface.

(2) With Cd content in the welding wires, there are more θ' phases precipitated in heat-treated α(Al). According to the analysis of precipitation thermodynamics and dynamics model, because of the higher vacancy binding energy of Cd, Cd-vacancy clusters are formed and provide a large number of nucleation locations for θ' phases, which decreases the nucleation energy of θ' phases. The higher diffusion coefficient of the Cd-vacancy cluster and the lower interfacial energy of θ' phase lead to

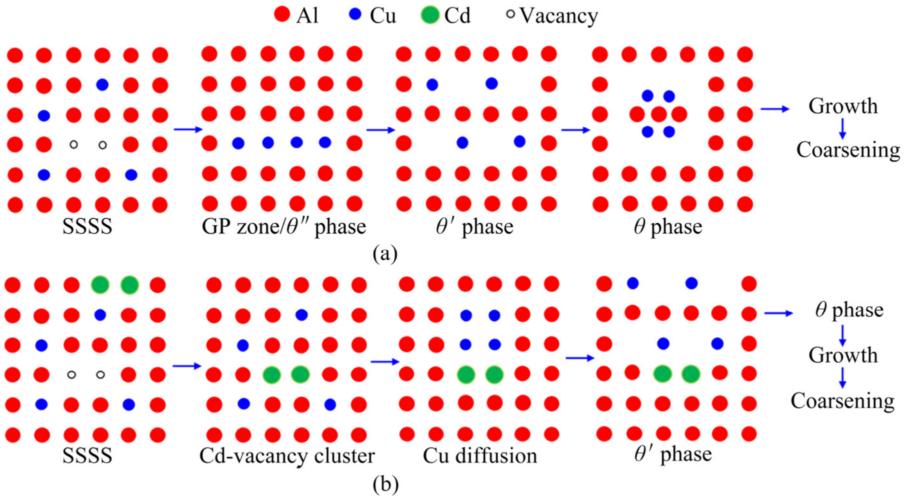

Fig. 11 Schematic diagrams of aging sequence in Al−Cu alloy (a) and Al−Cu−Cd alloy (b)

dense θ' phases. According to the strengthening model, after adding Cd in ER2319 welding wires, the yield strength increases by 43 MPa in the building direction of the heat-treated wall structures.

Acknowledgments

The authors would like to acknowledge the financial support from the National Key Technologies Research & Development Program of China (No. 2018YFB1106000) and the Youth Talent Project of CAST (No. 2019QNRC001).

References

[1] ZHANG Yi, WU Lin-min, GUO Xing-ye, KANE S, DENG Yi-fan, JUNG Y G, LEE J H, ZHANG Jing. Additive manufacturing of metallic materials: A review [J]. Journal of Materials Engineering Performance, 2017, 27: 1−13.

[2] BOURGEOIS L, DWYER C, WEYLAND M, NIE Jian-feng, MUDDLE B C. The magic thicknesses of θ' precipitates in Sn-microalloyed Al−Cu [J]. Acta Materialia, 2012, 60: 633−644.

[3] SUN Ru-jian, LI Liu-he, ZHU Ying, GUO Wei, PENG Peng, CONG Bao-qiang, SUN Jian-fei, CHE Zhi-gang, LI Bo, GUO Chao, LIU Lei. Microstructure, residual stress and tensile properties control of wire−arc additive manufactured 2319 aluminum alloy with laser shock peening [J]. Journal of Alloy and Compounds, 2018, 747: 255−265.

[4] SAFARZADE A, SHARIFITABAR M, AFARANI M S. Effects of heat treatment on microstructure and mechanical properties of Inconel 625 alloy fabricated by wire arc additive manufacturing process [J]. Transactions of Nonferrous Metals Society of China, 2020, 30: 3016−3030.

[5] DEREKAR K S. A review of wire arc additive manufacturing and advances in wire arc additive manufacturing of aluminium [J]. Material Science and Technology, 2018, 34: 895−916.

[6] GU Jiang-long, DING Jia-luo, WILLIAMS S W, GU Hui-min, BAI Jing, ZHAI Yu-chun, MA Pei-hua. The strengthening effect of inter-layer cold working and post-deposition heat treatment on the additively manufactured Al−6.3Cu alloy [J]. Material Science and Engineering A, 2016, 651: 18−26.

[7] ZHANG Xiao-yong, ZHOU Qi, WANG Ke-hong, PENG Yong, DING Jia-luo, KONG Jian, WILLIAMS S. Study on microstructure and tensile properties of high nitrogen Cr−Mn steel processed by CMT wire and arc additive manufacturing [J]. Materials and Design, 2019, 166: 1−15.

[8] HONNIGE J R, COLEGROVE P A, AHMED B, FITZPATRICK M E, GANGULY S, LEE T L, WILLIAMS S W. Residual stress and texture control in Ti−6Al−4V wire + arc additively manufactured intersections by stress relief and rolling [J]. Materials and Design, 2018, 152: 192−199.

[9] ARAUJO J, MILAGRE M, FERREIRA R, MACHADO C, ABREU C, COSTA I. Microstructural characteristics of the Al alloys: The dissimilarities among the 2XXX alloys series used in aircraft structures [J]. Metallography, Microstructure and Analysis, 2020, 9: 744−758.

[10] WANG Jian, LIU Zhi-yi, BAI Song, CAO Jing, ZHAO Juan-gang, ZENG Di-ping. Combined effect of Ag and Mg additions on localized corrosion behavior of Al−Cu alloys with high Cu content [J]. Journal of Materials Engineering and Performance, 2020, 29: 6108−6117.

[11] ZHOU Ying-hui, LIN Xin, KANG Nan, HUANG Wei-dong, WANG Jiang, WANG Zhe-nan. Influence of travel speed on microstructure and mechanical properties of wire + arc additively manufactured 2219 aluminum alloy [J]. Journal of Materials Science and Technology, 2020, 37: 143−153.

[12] DONG Ming-ye, ZHAO Yue, LI Quan, WANG Fu-de, Wu Ai-ping. Microstructure evolution and mechanical property anisotropy of wire and arc-additive-manufactured wall structure using ER2319 welding wires [J]. Journal of Materials Engineering and Performance, 2021 30: 258−268.

[13] QI Ze-wu, CONG Bao-qiang, QI Bo-jin, ZHANG Gang, DING Jia-luo. Properties of wire + arc additively manufactured 2024 aluminum alloy with different solution treatment temperature [J]. Materials Letter, 2018, 255: 347−353.

[14] BAI Jiu-yang, FAN Cheng-lei, LIN San-bao, YANG Chun-li, DONG Bo-Lun. Mechanical properties and fracture behaviors of GTA-additive manufactured 2219-Al after an especial heat treatment [J]. Journal of Materials Engineering Performance, 2017, 26: 1808−1816.

[15] GONG Yan-li, GAO Lin, LI Kai, DU Yong, SONG Min. Structural instability of plate-shaped θ' precipitates in an aged Al−Cu alloy [J]. Philosophical Magazine Letters, 2020, 100: 524−532.

[16] PAPAZIAN J M. A calorimetric study of precipitation in aluminum alloy 2219 [J]. Metallurgical Transactions A, 1981, 12: 269−280.

[17] CAO Yu-dong, CHEN Xiao-hua, WANG Zi-dong, CHEN Kai-xuan, TANG Wei-zhong, PAN Shi-wei, YANG Xing-hai, QIN Junwei, LI Shao-hua, WANG Wan-lin. Effect of Cd micro-addition on microstructure and mechanical properties in ternary Al−Si−Cu alloy [J]. Journal of Alloys and Compounds, 2020, 851: 156739.

[18] SILCOCK J M, FLOWER H M. Comments on a comparison of early and recent work on the effect of trace additions of Cd, In, or Sn on nucleation and growth of θ' in Al−Cu alloys [J]. Scripta Materialia, 2002, 46: 389−394.

[19] WANG Shuai, GU Hui-min, WANG wei, LI Cheng-de, REN Ling-ling, WANG Zhen-biao, ZHAI Yu-chun, MA Pei-hua. Microstructure and mechanical properties of ZL205A aluminum alloy wall produced by wire arc additive manufacturing [J]. Rare Metal Materials and Engineering, 2019, 48: 2910−2916.

[20] SANKARAN R, LAIRD C. Effect of trace additions Cd, In and Sn on interfacial structure and kinetics of growth of theta′ plates in Al−Cu alloy [J]. Material Science and Engineering A, 1974, 14: 271−279.

[21] RINGER S P, HONO K, SAKURA T. The effect of trace additions of Sn on precipitation in Al−Cu alloys−An atom-probe field-ion microscopy study [J]. Metallurgical and Materials Transactions A, 1995, 26: 2207−2217.

[22] NOBLE B. Theta-prime precipitation in aluminium−copper−cadmium alloys [J]. Acta Materialia, 1968, 16: 393−401.

[23] SUZUKI H, KANNO M, FUKUNAGA K. Studies on aging retardation in Al−Cu−Cd alloys [J]. Journal of Japan Institute Light Metals, 1972, 22: 599−604.

[24] YU J M, WANDERKA N, RACK A, DAUDIN R, BOLLER E, MARKOTTER H, MANZONI A, VOGEL F, ARLT T, MANKE I. Influence of impurities, strontium addition and cooling rate on microstructure evolution in Al−10Si−0.3Fe casting alloys [J]. Journal of Alloy and Compounds, 2018, 766: 818−827.

[25] LIN Bo, XU Rui, LI Hao-yu, XIAO Hua-qiang, ZHANG Wei-wen, LI Shao-bo. Development of high Fe content squeeze cast 2A16 wrought Al alloys with enhanced mechanical properties at room and elevated temperatures [J]. Materials Characterization, 2018, 139: 389−397.

[26] LIANG Xiao-peng, LI Hui-zhong, LI Zhou, TAO Hong, MA Bing, LIU Sheng-dan, LIU Yong. Study on the microstructure in a friction stir welded 2519-T87 Al alloy [J]. Materials and Design, 2012, 35: 603−608.

[27] LIU G, ZHANG G J, DING X D, SUN J, CHEN K H. Modeling the strengthening response to aging process of heat-treatable aluminum alloys containing plate/disc- or rod/needle-shaped precipitates [J]. Materials Science and Engineering A, 2003, 344: 113−124.

[28] QIAN Feng, ZHAO Dong-dong, MRTSELL E A, JIN Shen-bao, WANG Jun-sheng, MARIOARA C D, ANDERSEN S J, SHA Gang, LI Yan-jun. Enhanced nucleation and precipitation hardening in Al−Mg−Si(−Cu) alloys with minor Cd additions [J]. Material Science and Engineering A, 2020, 792: 139698.

[29] DESCHAMPS A, DECREUS B, GEUSER F D. The influence of precipitation on plastic deformation of Al−Cu−Li alloys [J]. Acta Materialia, 2013, 61: 4010−4021.

[30] DOLAN G P, ROBINSON J S. Residual stress reduction in 7175-T73, 6061-T6 and 2017A-T4 aluminium alloys using quench factor analysis [J]. Journal of Materials Processing Technology, 2003, 153: 346−351.

[31] LUO Sheng, WANG Gang, HU Yi-sen, ZHONG Yu, RONG Yi-ming. Effect of quenching rate and its coupling model on precipitation and strength of Al−Cu−Cd alloys [J]. Material Science and Engineering A, 2019, 761: 138022.

[32] HU Yi-sen, WANG Gang, JI Yan-zhou, WANG Li-ping, RONG Yi-ming, CHEN Long-qing. Study of θ' precipitation behavior in Al−Cu−Cd alloys by phase-field modeling [J]. Material Science and Engineering A, 2019, 746: 105−114.

焊丝中 Cd 元素的添加对电弧增材制造 Al−Cu 合金显微组织和力学性能的影响

董明晔 [1]，赵 玥 [1,2]，李 权 [3]，王福德 [3]，吴爱萍 [1,2,4]

1. 清华大学 机械工程系，北京 100084；
2. 清华大学 先进成形制造教育部重点实验室，北京 100084；
3. 首都航天机械有限公司，北京 100076；
4. 清华大学 摩擦学国家重点实验室，北京 100084

摘 要：利用含 Cd 和不含 Cd 的两种焊丝，基于冷金属过渡的电弧增材制造技术制造单壁墙。为提高力学性能，对单壁墙进行 T6 热处理。由于 Cd 具有较高的空位结合能，在时效阶段形成的大量 Cd-空位团簇为θ'相提供大量形核位置，从而降低θ'相的形核能。Cd-空位团簇的高扩散系数和θ'相的低界面能促使热处理态 α(Al)中细密θ'相的形成。根据强化模型，在 ER2319 焊丝中添加 Cd 后，热处理态单壁墙增材方向的屈服强度提高 43 MPa。

关键词：Cd；焊丝；电弧增材制造；铝铜合金

(Edited by Bing YANG)